Extreme Mechanics Letters 58 (2023) 101929

Contents lists available at ScienceDirect

Extreme Mechanics Letters

journal homepage: www.elsevier.com/locate/eml

Atomistic insights into the mechanical anisotropy and fragility of monolayer fullerene networks using quantum mechanical calculations and machine-learning molecular dynamics simulations

Penghua Ying [a], Haikuan Dong [b,c], Ting Liang [d], Zheyong Fan [b], Zheng Zhong [a,*], Jin Zhang [a,*]

[a] School of Science, Harbin Institute of Technology, Shenzhen, 518055, PR China
[b] College of Physical Science and Technology, Bohai University, Jinzhou, 121013, PR China
[c] Beijing Advanced Innovation Center for Materials Genome Engineering, University of Science and Technology Beijing, Beijing, 100083, PR China
[d] Department of Electronic Engineering and Materials Science and Technology Research Center, The Chinese University of Hong Kong, Shatin, N.T., 999077, Hong Kong Special Administrative Region of China

ARTICLE INFO

Article history:
Received 6 September 2022
Received in revised form 27 October 2022
Accepted 18 November 2022
Available online 21 November 2022

Keywords:
Monolayer fullerene network
Neuroevolution potential
Fracture behavior
Molecular dynamics
Tensile property

ABSTRACT

In this work, we comprehensively study the mechanical properties of the newly synthesized monolayer quasi-hexagonal-phase fullerene (qHPF) membrane [Hou et al., 2022] under uniaxial tension by using quantum mechanical density-functional-theory (DFT) calculations and molecular dynamics (MD) simulations with a machine-learned neuroevolution potential (NEP). The elastic properties and fracture behaviors of monolayer qHPF are found to be strongly anisotropic due to the different properties between the inter-fullerene C–C single bonds and [2 + 2] cycloaddition bonds. Moreover, the tensile strength and fracture strain of monolayer qHPF are much smaller than those of any other existing two-dimensional (2D) carbon crystals. The very small tensile strength or fracture strain is ascribed to the inhomogeneous deformation of the stretched monolayer qHPF, which originates from the stiffness difference between the soft inter-fullerene bonds and the rigid intra-fullerene bonds. Compared with DFT calculations at the ground state, the NEP-based extensive MD simulations predict a much smaller tensile strength and fracture strain for monolayer qHPF due to their consideration of the effects of temperature and membrane size. Our work not only reveals the underlying mechanism of the fracture behaviors of monolayer fullerene networks from an atomistic perspective, but also shows the effectiveness and accuracy of the NEP approach in determining the mechanical properties of 2D materials in the realistic situations.

© 2022 Elsevier Ltd. All rights reserved.

1. Introduction

Carbon is one of the most important elements for life on earth due to its diverse electronic hybridization characteristics. As two traditional carbon allotropes, diamond and graphite are well recognized to possess different properties, due to the diverse chemical bonds in their lattice structures. The diversity in the physical properties of diamond and graphite together with the ability of carbon to form sp-, sp^2-, and sp^3-hybridized bonds has inspired the search for new allotropes of carbon. Within the last few decades, various low-dimensional carbon materials have been discovered, which include zero-dimensional fullerene [1], one-dimensional (1D) carbyne [2], quasi-1D carbon nanotubes [3], two-dimensional (2D) graphene [4], to name a few. These low-dimensional carbon materials are reported to have many unique properties superior to the convectional diamond and graphite. For instance, fullerene treated with alkali metals can become a high-T_c superconductor [5]. Carbon nanotube can be either metallic or semiconducting, depending on its chirality and diameter [6]. Graphene has been experimentally measured as one of the strongest materials with the Young's modulus of ∼1 TPa and tensile strength of ∼100 GPa [7]. Furthermore, the carbyne with linear atomic chain was theoretically predicted to have much higher gravimetric strength and toughness when compared with graphene and carbon nanotube [8,9]. Owing to these excellent properties, low-dimensional carbon materials are currently receiving the most attention from the community of chemistry, materials science, and condensed matter physics [10,11].

The newly discovered low-dimensional carbon materials also can serve as building blocks to construct novel carbon superarchitectures, which can be treated as a feasible bottom-up synthesis approach to obtain new carbon allotropes possibly with superior properties [12–15]. Both theoretical and experimental studies indicated that carbon nanotubes under high pressure or treated

* Corresponding authors.
E-mail addresses: zhongzheng@hit.edu.cn (Z. Zhong), jinzhang@hit.edu.cn (J. Zhang).

https://doi.org/10.1016/j.eml.2022.101929
2352-4316/© 2022 Elsevier Ltd. All rights reserved.

with electron beam welding can be connected covalently to form polymerized carbon structures, which not only partially retain some remarkable material properties of carbon nanotubes but also offer a class of 2D or three-dimensional (3D) structures with extraordinary structural properties such as ultrahigh porosity [16,17]. An exceptionally stable carbon honeycomb was reported recently, which can be treated as the 3D carbon superarchitecture constructed by the elements of graphene [18,19]. The carbon honeycomb or 3D graphene is reported to possess high porosity and accessibility, which is thus proven to have the high storage capacity for gas molecules [18]. Very recently, by merging cluster cages of C_{60} fullerenes through planar covalent carbon–carbon bonds, a new 2D carbon material, namely the quasi-hexagonal-phase fullerene (qHPF) has been fabricated in laboratory successfully [20]. This 2D fullerene polymer is reported to have a moderate bandgap and unique topological structure, both of which make this new material appealing for applications in 2D electronic devices [20]. Actually, the synthesis of 2D fullerene polymers can be dated back to 1995, when Iwasa et al. [21] reported the rhombohedral phase of C_{60} by high pressure synthesis. Since then, many theoretical efforts have been made to reveal the properties of 2D C_{60} polymers, which mainly focus on their structural stability and electronic properties [22–24]. However, not enough attention has been paid to the mechanics of 2D C_{60} polymers, which should play a key role in determining the structural integrity of the recently synthesized qHPF [25,26]. Moreover, the mechanical properties of qHPF are also of great importance for the proper functioning of qHPF-based devices, since the strain engineering is usually an efficient method to modify the properties of 2D materials [27–31]. Thus, the success of qHPF-based electronic devices crucially relies on a comprehensive understanding of the mechanical properties of the component qHPF.

From a theoretical perspective of atomistic simulations, the mechanical properties of 2D materials can be predicted by either quantum mechanical density-functional-theory (DFT) calculations or classical molecular dynamics (MD) simulations with an empirical potential. However, both approaches have their limitations. Although the DFT approach is very accurate, it cannot consider the effects of membrane size and finite temperature. The existing empirical potentials cannot fully hold their accuracy in describing new carbon allotropes such as qHPF synthesized recently, because most of them are specifically parameterized for some conventional carbon structures such as diamond and graphene. Recently, by training against the quantum mechanical DFT data, the machine-learned potentials (MLPs) have been shown to be a promising on-demand approach to investigate the mechanical properties of 2D materials. The MLP-driven MD simulations have been applied to study the negative Poisson's ratio of graphene [32], nanoscale tribology of graphene interfaces [33], and the elastic and fracture properties of monolayer BC_2N [34] and in-plane graphene/borophene junctions [35].

In this paper, using the results from DFT calculations as the training reference data, we construct an accurate MLP based on the neuroevolution potential (NEP) framework [36–38] to investigate the mechanical behaviors of monolayer qHPF under uniaxial tension. Based on DFT calculations and MLP-based MD simulations, the monolayer qHPF is found to be fragile with anisotropic fracture behaviors. In other words, the tensile strength and fracture strain of monolayer qHPF are much smaller than other existing 2D carbon allotropes. The very small fracture strain is attributed to the inhomogeneous deformation in the stretched monolayer qHPF, in which the local strain of soft inter-fullerene covalent bonds is much larger than that of the rigid fullerene. The strongly anisotropic mechanical property of monolayer qHPF originates from the distinct properties of the inter-fullerene covalent bonds in different directions. In addition, the impacts of size, temperature and strain rate on the mechanical properties of monolayer qHPF are also carefully examined by MLP-based MD simulations, which should be taken into account in the practical applications such as the strain engineering of the electronic property of qHPF.

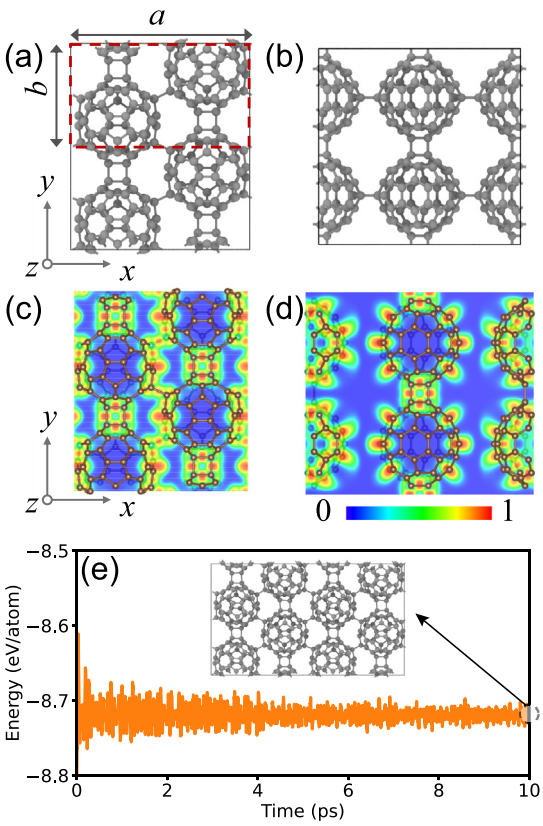

Fig. 1. (a–b) The initial crystal structures of monolayer (a) qHPF and (b) qTPF constructed using the lattice parameters from Ref. [20]. Here, a and b are the primitive lattice constants along x and y axes of qHPF, respectively. (c–d) The ELF of the optimized monolayer (c) qHPF and (d) qTPF. (e) Total energy evolution of $1 \times 2 \times 1$ supercells of monolayer qHPF at 800 K calculated by AIMD simulations. The inset shows the structure extracted at the end of AIMD simulations. For clarity, the $2 \times 2 \times 1$ supercell is presented here. The VESTA [39] and OVITO [40] packages were used for visualization of ELF and atomistic structures, respectively.

2. Models and methods

2.1. Atomistic models

Fig. 1(a) show the atomistic model of monolayer qHPF. In qHPF, each C_{60} molecule is linked with six neighboring C_{60} molecules with covalent bonds to form a 2D network structure. There are two types of inter-fullerene bonds in qHPF, wherein the covalent [2 + 2] cycloaddition bonds are along the [010] direction and the C–C single bonds are along the [110] and the [1$\bar{1}$0] directions. In addition to qHPF, another single-crystal fullerene polymer that is namely quasi-tetragonal-phase fullerene (qTPF) was also synthesized in the same experiment [20]. However, different from qHPF possessing the stable monolayer structure, the thinnest qTPF flakes fabricated in experiments are still few-layer. Thus, monolayer qTPF is expected to be unstable in atmosphere condition and under room temperature. To prove this deduction, the monolayer qTPF was also considered in DFT studies. For qTPF, each C_{60} molecule is linked with four neighboring C_{60} molecules with two covalent [2 + 2] cycloaddition bonds along the [010]

direction and two C–C single bonds along the [100] direction. The initial crystal structures of qHPF and qTPF were obtained from Ref. [20].

2.2. DFT calculations

All DFT calculations were performed using the VASP package [41] with the exchange–correlation PBE functional [42]. The energy cutoff for the projector augmented wave [43] was set as 520 eV. A Gaussian smearing with a width of 0.1 eV was used. The energy threshold of electronic self-consistent loop was set as 1×10^{-5} eV, while the force threshold of structural optimization was set as 1×10^{-2} eV/Å. The k-point mesh with a density of 0.25/Å was sampled in the in-plane Brillouin zone of the unit cell. A vacuum spacing of 20 Å was added in the direction perpendicular to the basal plane to isolate the monolayer qHPF or qTPF. In addition to the static calculations at ground state, AIMD simulations at finite temperatures were also performed to verify the thermodynamic stability of monolayer qHPF. In doing this, a $1 \times 2 \times 1$ supercell of qHPF was simulated within the NVT ensemble for 10 ps by using the Nosé–Hoover thermostat at 800 K, a time-step of 1 fs, and a $1 \times 1 \times 1$ k-point mesh. For reference datasets used in training and testing of NEP model, we adopted a higher energy cutoff (650 eV) and energy threshold of electronic self-consistent loop (1×10^{-8} eV). In the present DFT calculations and the following MD simulations, the thickness of monolayer qHPF was set as 8.78 Å for all stress calculations, which equals the layer separation in bulk qHPF [20].

2.3. The NEP framework

An MLP based on the NEP framework [36–38] was developed in this work to study the mechanical behaviors of qHPF under uniaxial tension. Based on a neural network, the NEP was trained via the separable natural evolution strategy (SNES) [44] against the reference dataset including energy, force, and virial values obtained from DFT calculations. Following the standard Behler–Parrinello high-dimensional neural network approach [45], the site energy U_i of an atom i is taken as a function of $N_{\rm des}$ descriptor components with the following form:

$$U_i = \sum_{\mu=1}^{N_{\rm neu}} w_\mu^{(1)} \tanh\left(\sum_{\nu=1}^{N_{\rm des}} w_{\mu\nu}^{(0)} q_\nu^i - b_\mu^{(0)}\right) - b^{(1)}, \tag{1}$$

where $N_{\rm neu}$ is the number of neurons, $\mathbf{w}^{(0)}$ and $\mathbf{w}^{(1)}$ are the trainable weights, $\mathbf{b}^{(0)}$ and $b^{(1)}$ are the bias parameters, and $\tanh(x)$ is the activation function.

In the NEP, the descriptor consists of a set of radial and angular components. The radial descriptor components q_n^i ($0 \le n \le n_{\rm max}^{\rm R}$) are constructed as

$$q_n^i = \sum_{j \neq i} g_n(r_{ij}), \tag{2}$$

where the summation runs over all the neighbors of atom i within a certain cutoff distance.

For the angular descriptor components, herein we considered the following many-body terms up to the fourth order [38], including three-body terms q_{nl}^i ($0 \le n \le n_{\rm max}^{\rm A}$, $1 \le l \le l_{\rm max}^{\rm 3b}$) and four-body terms $q_{nl_1l_2l_3}^i$ ($0 \le n \le n_{\rm max}^{\rm A}$, $1 \le l_1 = l_2 = l_3 \le l_{\rm max}^{\rm 4b}$):

$$q_{nl}^i = \sum_{m=-l}^{l} (-1)^m A_{nlm}^i A_{nl(-m)}^i, \tag{3}$$

$$q_{nl_1l_2l_3}^i = \sum_{m_1=-l_1}^{l_1} \sum_{m_2=-l_2}^{l_2} \sum_{m_3=-l_3}^{l_3} \begin{pmatrix} l_1 & l_2 & l_3 \\ m_1 & m_2 & m_3 \end{pmatrix} \times A_{nl_1m_1}^i A_{nl_2m_2}^i A_{nl_3m_3}^i, \tag{4}$$

where,

$$A_{nlm}^i = \sum_{j \neq i} g_n(r_{ij}) Y_{lm}(\theta_{ij}, \phi_{ij}). \tag{5}$$

Here, $Y_{lm}(\theta_{ij}, \phi_{ij})$ is the spherical harmonic, which is a function of the polar angle θ_{ij} and the azimuthal angle ϕ_{ij} for the position difference vector $\boldsymbol{r}_{ij} \equiv \boldsymbol{r}_j - \boldsymbol{r}_i$ between atoms i and j.

The radial functions $g_n(r_{ij})$ in Eq. (2) are defined as a linear combination of $N_{\rm bas}^{\rm R} + 1$ basis functions $\{f_k(r_{ij})\}_{k=0}^{N_{\rm bas}^{\rm R}}$:

$$g_n(r_{ij}) = \sum_{k=0}^{N_{\rm bas}^{\rm R}} c_{nk}^{ij} f_k(r_{ij}), \quad \text{with} \tag{6}$$

$$f_k(r_{ij}) = \frac{1}{2}\left[T_k\left(2\left(r_{ij}/r_{\rm c}^{\rm R} - 1\right)^2 - 1\right) + 1\right] f_{\rm c}(r_{ij}). \tag{7}$$

Here, $T_k(x)$ is the kth order Chebyshev polynomial of the first kind and $f_{\rm c}(r_{ij})$ is the cutoff function defined as

$$f_{\rm c}(r_{ij}) = \begin{cases} \frac{1}{2}\left[1 + \cos\left(\pi \frac{r_{ij}}{r_{\rm c}^{\rm R}}\right)\right], & r_{ij} \le r_{\rm c}^{\rm R}; \\ 0, & r_{ij} > r_{\rm c}^{\rm R}. \end{cases} \tag{8}$$

Here, $r_{\rm c}^{\rm R}$ is the cutoff distance of the radial descriptor components. The trainable expansion coefficients c_{nk}^{ij} depend on n, k and also the types of atoms i and j. The functions $g_n(r_{ij})$ in Eq. (5) have the similar definition except for the different basis size $N_{\rm bas}^{\rm A}$ and the different cutoff distance $r_{\rm c}^{\rm A}$.

During the training process, the total loss function is minimized to optimize the free parameters in the NEP model using the SNES. The total loss function is defined as a weighted sum of several individual ones:

$$L = \lambda_1 L_1 + \lambda_2 L_2 + \lambda_{\rm e} \Delta U + \lambda_{\rm f} \Delta F + \lambda_{\rm v} \Delta W \tag{9}$$

where ΔU, ΔF, and ΔW are the root mean square errors (RMSEs) of energy, force, and virial, respectively, between the predicted and the reference values, L_1 and L_2 are proportional to the 1-norm and 2-norm of the training parameters, and $\lambda_{\rm e}$, $\lambda_{\rm f}$, $\lambda_{\rm v}$, λ_1, λ_2 are the weights of the various terms. For more details on the NEP approach, we refer the readers to the original papers [36–38].

2.4. The MLP-based tensile simulations

In addition to DFT calculations, MLP-based MD simulations were utilized here to conduct the tensile simulations of the monolayer qHPF membrane. All MD simulations were performed by using the GPUMD package (version 3.3.1) [46] with a time step of 1 fs. The periodic boundary conditions were applied along both planar directions. During the simulations, the system was firstly relaxed within the isothermal–isobaric (NpT) ensemble at the target temperature and zero external pressure using the Berendsen thermostat and barostat [47] for 100 ps. Afterward, the qHPF membrane was stretched in the x or y direction with a specific strain rate. The temperature was controlled using the Bussi–Donadio–Parrinello thermostat [48], while the target stress along the lateral direction was controlled at zero using the stochastic cell rescaling barostat [49]. The effects of size (ranging from 5 nm × 5 nm to 44 nm × 44 nm), temperature (ranging from 100 K to 800 K), and strain rate (ranging from 1×10^7/s to 1×10^9/s) on the mechanical properties were studied.

3. Results and discussion

In this section, the mechanical properties of monolayer fullerene networks are investigated by aforementioned DFT calculations and MLP-based MD simulations. Specifically, DFT calculations are majorly employed to reveal the fracture mechanism of

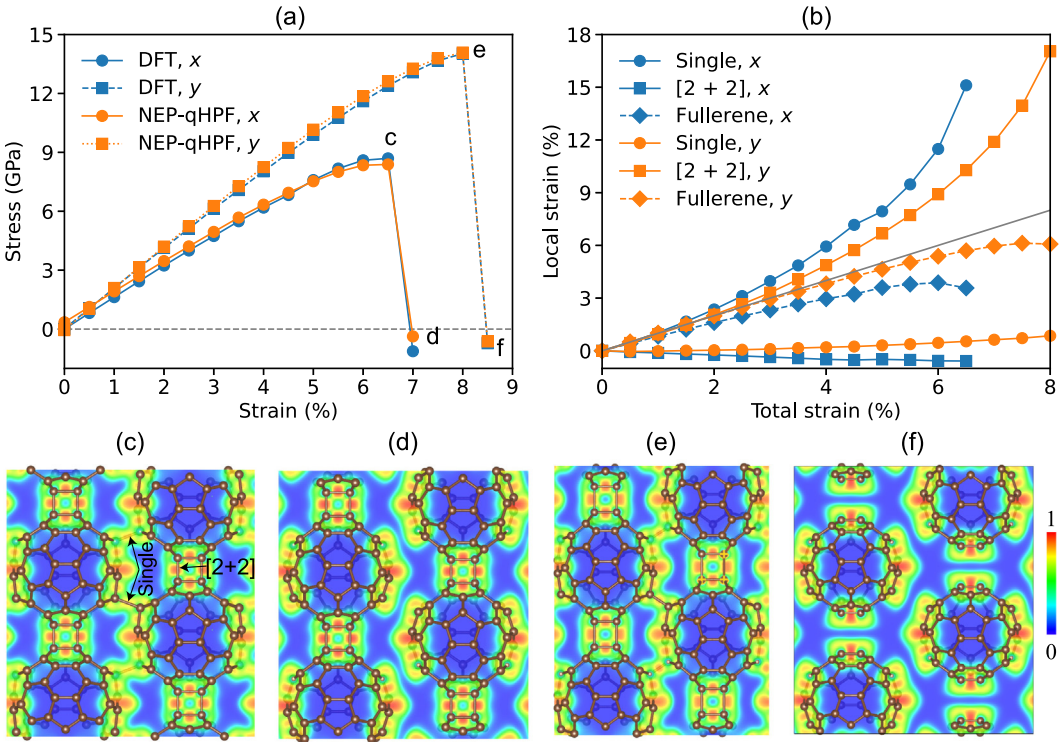

Fig. 2. (a) The stress–strain curves of monolayer qHPF under uniaxial tension predicted by DFT calculations and NEP-qHPF model. (b) Deformations of inter-fullerene covalent bonds (C–C single and [2 + 2] cycloaddition bonds) and individual fullerenes with increasing total strain. Here, the local strains of inter-fullerene covalent bonds were calculated as the ratios of bond length increments to the initial bond lengths as marked in (c). (c–f) The ELFs of four representative structures before and after the fracture, as labeled in (a).

monolayer fullerene networks at ground state. In MD simulations with the accurate NEP model, samples with a larger number of atoms and the dynamics factors such as the temperature effect and loading rate can be taken into account, which are demonstrated to play an important role in determining the tensile strength and fracture strain of monolayer qHPF.

3.1. DFT calculation results

In Fig. 1(c) and (d), we illustrate the electron localization function (ELF) [50] of both monolayer qHPF and qTPF after the structural optimization. Here, the value of ELF ranging between 0 and 1 is a spatial function that describes the atomic bonding characteristics of fullerene polymers. The optimized qHPF is found to retain its covalently bonded 2D network structure, since electron localization occurs around the center of all bonds, indicating the dominance of covalent bonding between pairs of carbon atoms. The lattice constants a and b of qHPF as shown in Fig. 1(a) are predicted to be 15.91 Å and 9.16 Å, respectively, both of which are very close to the experimental results (16.00 Å and 9.17 Å). However, although covalent [2 + 2] cycloaddition bonds connecting neighboring fullerenes in the y direction retain in qTPF after the structural optimization, the C–C single bonds between fullerenes in the x direction disappear after this treatment, making monolayer qTPF transfer into a series of parallel 1D linear C_{60}. This result suggests that the monolayer qTPF is indeed unstable, which is thus excluded from the present study.

To further validate the thermodynamic stability of monolayer qHPF, especially when it is used under a relatively high temperature, AIMD simulations were conducted for the monolayer qHPF. As shown in Fig. 1(e), the energy fluctuates around a stable average value during the AIMD simulation. Moreover, the monolayer qHPF obtained after the AIMD simulation is structurally similar to its initial configuration without any bond breakage. These results indicate the thermodynamic stability of the monolayer qHPF. Thus, only monolayer qHPF was considered in the following study.

In Fig. 2, we show the stress–strain relations of monolayer qHPF uniaxially elongated with a small strain increment of 0.5% each step along x and y directions. In each step, the stress along the lateral direction (perpendicular to the loading direction) was released to zero. At the beginning, stress and strain exhibit a linear relationship, giving the tensile modulus as the slope of the linear stress–strain curves with strain less than 1%. Thus, according to Fig. 2, the tensile modulus of monolayer qHPF in the x direction is predicted as 162.8 GPa, which is much smaller than 207.0 GPa in the y direction. As the strain grows, the stress–strain curve experiences a nonlinear response until the ultimate tensile strength, at which monolayer qHPF reaches its maximum bearing load. By further loading monolayer qHPF after the tensile strength, the stress drops to zero abruptly, which indicates the occurrence of brittle failure. We find that the fracture properties of monolayer qHPF are also anisotropic. Specifically, the tensile strength and fracture strain in the y direction are, respectively, 14.1 GPa and 8.0%, which are both larger than the values of 8.9 GPa and 6.5% in the x direction. Here, the fracture strain is another important mechanical parameter measuring the deformation capacity of a stretched material before the nucleation of cracks, which is defined as the strain at the point where the stress reaches the tensile strength. In Fig. 3, we compare the fracture properties of monolayer qHPF with some other 2D carbon allotropes and related 2D materials. Both the tensile strength and fracture strain of the present monolayer qHPF are found to be much smaller than those of most other 2D materials, indicating the mechanical fragility of monolayer qHPF under tension. Notably, this mechanical fragility could also contribute to the relatively larger ratio of elastic modulus to tensile strength when compared with other 2D carbon allotropes such as graphene.

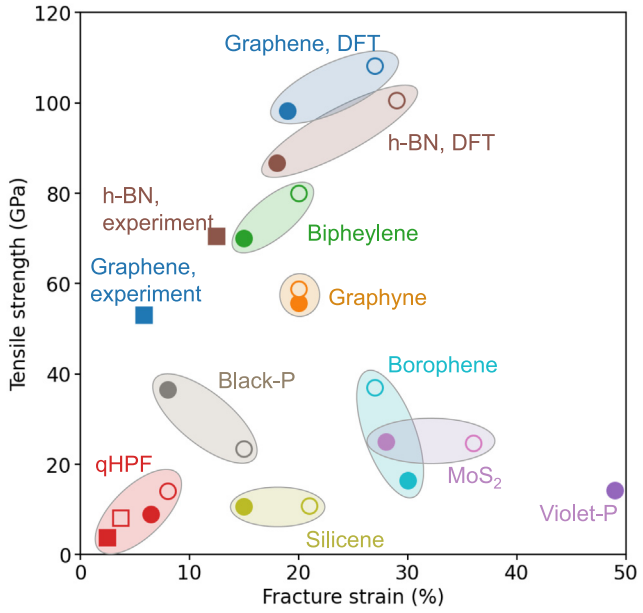

Fig. 3. A comparison of the tensile strength and fracture strain between monolayer qHPF and other 2D materials including graphene [51,52], *h*-BN (hexagonal boron nitride) [53,54], graphyne [55], biphylene network [56], bophorene [57], silicene [58], Black-P (black phosphorene) [59], Violet-P (violet phosphorene) [28], and MoS_2 (molybdenum disulfide) [60]. Here, the hollow and solid circles denote the DFT results in the armchair and zigzag directions (or the strongest and weakest directions), respectively. The squares of graphene and *h*-BN are experimental results, while the squares of qHPF are results predicted by MLP-based MD simulations.

In addition to fracture properties, the elastic properties of qHPF are also investigated (see Section S1 in Supplemental Material). We find that the monolayer qHPF has a much smaller elastic modulus but a much higher elastic anisotropy than any other already synthesized 2D carbon allotropes.

To better explain the fragile property observed in monolayer qHPF and better reveal its deformation mechanism during the tension process, in Fig. 2(b) we show the local strain evolution of inter-fullerene C–C single bonds, [2 + 2] cycloaddition bonds and individual fullerenes during the tension process in both *x* and *y* directions. In general, a significant inhomogeneous deformation is observed in the monolayer qHPF, since the elongation of the inter-fullerene bonds is much larger than that of the intra-fullerene bonds. This fact explains the very small fracture strain of monolayer qHPF, because the stretching of monolayer qHPF majorly results in the elongation of the soft inter-fullerene bonds. Moreover, the larger tensile strength and fracture strain observed in the *y* direction of monolayer qHPF can be attributed to the effect of stronger [2 + 2] cycloaddition bonds as described above, since the loading in the *y* direction is majorly resisted by [2 + 2] cycloaddition bonds, while the loading in the *x* direction is mainly resisted by C–C single bonds.

The deformation process together with the corresponding ELFs of monolayer qHPF stretched along *x* and *y* directions are illustrated in Fig. 2(c–f). Here, structures at the fracture strength point and shortly after the rupture are shown here as two important representative statuses. A comparison among the ELFs just before and after the rupture indicates that monolayer qHPF stretched along *x* and *y* directions should exhibit different cracking characteristics. When stretched along the *x* direction, only the C–C single bonds connecting neighboring fullerenes are broken after the rupture but the [2 + 2] cycloaddition bonds parallel to the loading direction are kept intact. After the loading direction shifts to the *y* direction, elongations of the straight [2 + 2] cycloaddition bonds and the inclined C–C single bonds both contribute to the overall deformation of monolayer qHPF. Since the C–C single bonds are much weaker than the [2 + 2] cycloaddition bonds, the breaking of the latter will consequently trigger the breaking of the former. Thus, both the [2 + 2] cycloaddition bonds and C–C single bonds are broken in the ruptured qHPF when it is stretched along the *y* direction. Based on the above findings, it is expected that the crack in the monolayer qHPF stretched along the *x* direction will show a straight line that is exactly perpendicular to the loading direction, while the structures stretched along the *y* direction will have a more complicated crack growth path making the crack have a more complicated pattern.

In section S2 (see Supplemental Material), we also show the strain effect on the electronic band structures of monolayer qHPF. Due to the splitting of both valence band maximum and conduction band maximum near the Γ point under tensile strain, a significant reduction is observed in the band gap of the stretched monolayer qHPF regardless of the loading direction. However, as we will discuss later, because DFT calculations usually cannot consider the effects of temperature and membrane size, this method will significantly overestimate the fracture property of monolayer qHPF in the realistic environment. The fracture behaviors of the monolayer qHPF membrane stretched at the finite temperature will be further discussed using extensive MD simulations as introduced in Section 2.4.

3.2. NEP model for monolayer qHPF

3.2.1. Generation of training and testing datasets

Very recently, some researchers have developed an NEP model for amorphous carbon [38], which is denoted as NEP-Carbon in the present work. Nevertheless, its training dataset mainly consists of the crystal diamond and graphite, liquid and amorphous carbon structures [61]. To accurately describe the mechanical behavior of the newly synthesized monolayer qHPF, we developed here a new NEP model, namely, NEP-qHPF. Because the monolayer qHPF is stable in MD simulations with the NEP-Carbon model [62], we used this model as a pre-trained model to accelerate the sampling of reference structures. The training and testing structures of qHPF were obtained from three parts including MD simulations near the equilibrium state, uniaxial tension based on MD simulations, and uniaxial tension based on DFT calculations. All simulations were performed with the primitive cell of qHPF containing 120 atoms.

For MD simulations near the equilibrium state, we used the NEP-Carbon model to run *NpT* simulations by using the Bussi–Donadio–Parrinello thermostat [48] and the stochastic cell rescaling barostat [49]. Three target pressures including 0 GPa, 1 GPa, and −1 GPa in both *x* and *y* directions were considered. For each target pressure, we linearly increased the target temperature from 10 K to 1000 K during a simulation period of 2500 ps. We sampled the structures every 50 ps, resulting in 50 structures obtained for each target pressure. Therefore, 150 structures were collected in total.

For uniaxial tension based on MD simulations, the simulation details have been introduced in Section 2.4. Five target temperatures including 100 K, 300 K, 500 K, 700 K, and 900 K in both *x* and *y* directions were considered. For each temperature, the primitive cell of qHPF was uniaxially stretched in *x* and *y* directions with a strain rate of 1×10^8/s until fracture. We obtained 100 structures in total by extracting 10 structures for each uniaxial tension simulation.

For uniaxial tension based on DFT simulations, the monolayer qHPF was elongated with a small strain increment of 0.5% each

Table 1
Hyperparameters for the NEP-qHPF model.

Parameter	Value	Parameter	Value
r_c^R	4.2 Å	r_c^A	3.7 Å
n_{max}^R	10	n_{max}^A	8
N_{bas}^R	10	N_{bas}^A	8
l_{max}^{3b}	4	l_{max}^{4b}	2
N_{neu}	50	λ_1	0.1
λ_2	0.1	λ_e	1.0
λ_f	1.0	λ_v	0.5
N_{bat}	240	N_{pop}	50
N_{gen}	9×10^5		

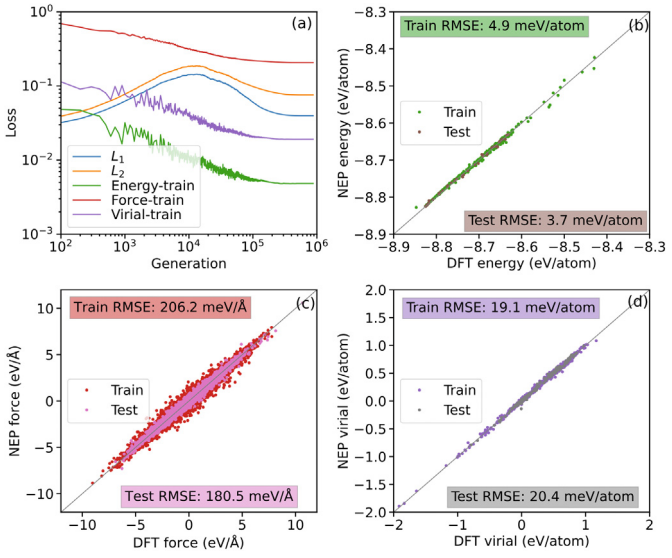

Fig. 4. (a) The evolution of various loss functions for the qHPF training dataset with respect to the generation. (b) Energy, (c) force, and (d) virial calculated from NEP as compared to the DFT reference data for the training and testing datasets.

step along the x or y direction. In each step, the stress along the lateral direction (perpendicular to the loading direction) was released to zero. In total, 30 structures were obtained after we extracted 15 structures for each uniaxial tension simulation.

Overall, 280 structures have been obtained in total. Specifically, 240 structures (28 800 atoms) of them were randomly selected to generate the training dataset, while the other 40 structures (4800 atoms) formed the testing dataset. We further used DFT calculations to obtain the energy, force, and virial data of these structures, which were taken as the input reference dataset for NEP-qHPF model training.

3.2.2. NEP model training and validating

We employed the GPUMD package (version 3.3.1) [38,46] to train the NEP-qHPF model with the hyperparameters listed in Table 1. The hyperparameters used here for the NEP-qHPF model are generally consistent with those for the NEP-Carbon model [38] except for the following three modifications. First, the five-body descriptor components as defined in Ref. [38] have not been included. Second, we have increased the regularization weights, ℓ_1 and ℓ_2 from 0.05 to 0.1, which can help to increase the robustness of the potential in MD simulations. Third, we have increased the virial weight, λ_v from 0.1 to 0.5, which is expected to increase the accuracy of NEP-qHPF in predicting the mechanical properties of monolayer qHPF.

Fig. 4(a) shows the evolution of various loss functions for the qHPF training dataset with respect to generations. The training

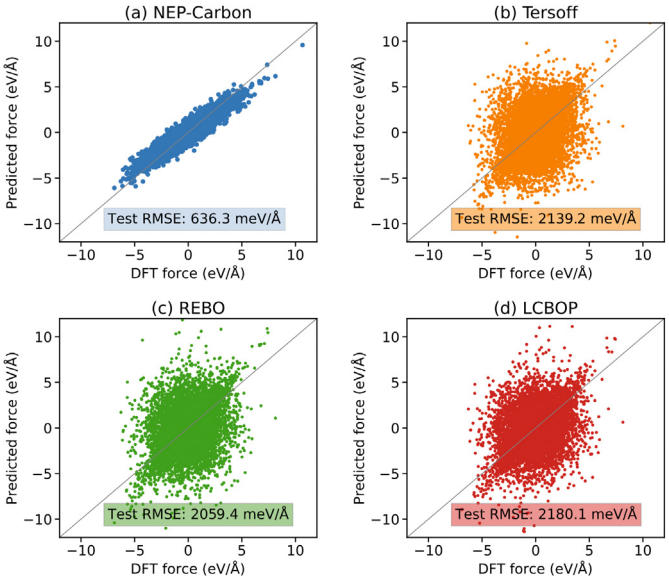

Fig. 5. Force calculated from (a) NEP-Carbon, (b) Tersoff, (c) REBO, and (d) LCBOP as compared to the DFT reference data for the test dataset.

has been performed for 9×10^5 generations with all loss functions being completely converged. The corresponding energy, force, and virial predicted by NEP-qHPF are compared against the DFT reference values in Fig. 4(b)–(d), respectively. The RMSEs for train and test datasets are presented. For the purpose of comparison, in Fig. 5 we also evaluate the accuracy of the previous NEP-Carbon model and some popular empirical potentials for the carbon system including the Tersoff potential [63,64], REBO potential [65], and LCBOP potential [66] by comparing their predicted forces for the test dataset against the DFT reference values. It can be clearly seen that our NEP-qHPF model with RMSE of 206.2 meV/Å shows the highest accuracy among all the potentials. Moreover, the NEP-qHPF model can also well reproduce the tensile curves predicted by DFT calculations as shown in Fig. 2. The force RMSE of the previous NEP-carbon model is 636.3 meV/Å, which is less accurate than the NEP-qHPF model but is still much more accurate than the empirical potentials. For all empirical potentials, most parts of predicted forces deviate from the parity line and the corresponding RMSEs are larger than 2000 meV/Å.

In Table 2 we compare the lattice constants and inter-fullerene bond lengths predicted by different potentials. The two NEP models show a much higher accuracy than the empirical ones in predicting both the lattice constants and inter-fullerene bond lengths. Moreover, the inter-fullerene bond lengths predicted by the NEP-qHPF model perfectly agree with the DFT values. To further check the reliability of the NEP-qHPF model in the tensile simulations at finite temperatures, we compare the distribution in the latent space [67] for structures under tensile loading obtained from MD simulations and the training structures in Fig. 6. Following the definitions in Ref. [38], the high-dimensional latent space can be effectively reduced by PC analysis. It can be seen that all stretched structures sampled from MD simulations are totally within the region spanned by the training dataset, indicating the reliability of NEP-qHPF in describing the fracture behaviors of monolayer qHPF. From the above findings, we expect that the high accuracy of the NEP-qHPF model can lead to a reliable prediction of the mechanical properties of qHPF as discussed in the remainder of this paper.

Table 2
Equilibrium lattice constants and inter-fullerene bond lengths of monolayer qHPF predicted by the various potentials and DFT calculations. Here, a and b are the lattice constants along the x and y directions, respectively. l_1 and l_2 are the lengths of the C–C single bonds and the [2+2] cycloaddition bonds, respectively.

Approach	a (Å)	b (Å)	l_1 (Å)	l_2 (Å)
DFT	15.91	9.16	1.61	1.61
NEP-qHPF	15.88	9.19	1.61	1.61
NEP-Carbon	15.88	9.18	1.55	1.59
Tersoff	16.51	9.47	1.52	1.61
REBO	15.92	9.25	1.51	1.61
LCBOP	16.28	9.25	1.50	1.41

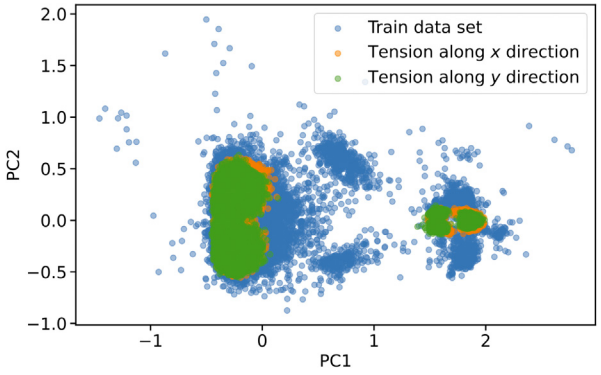

Fig. 6. Distribution of training structures and structures under tension in the 2D PC space (spanned by PC 1 and PC 2) as reduced from the latent space using the PYNEP package [38]. Here, structures under tension were sampled from tensile simulations of monolayer qHPF containing 960 atoms at 300 K with a strain rate of 1×10^8/s along x and y directions.

3.3. MLP-based MD simulation results

3.3.1. Size effect

Using extensive MLP-based MD simulations, in Fig. 7(a) we show the strain–stress curves of the monolayer qHPF uniaxially stretched along x and y directions with a strain rate of 1×10^8/s at room temperature of 300 K. Here, five square monolayer qHPF membranes with different sizes of 5 nm × 5 nm (containing 1800 atoms), 11 nm × 11 nm (10 080 atoms), 22 nm × 22 nm (40 320 atoms), 33 nm × 33 nm (90 720 atoms), and 44 nm × 44 nm (containing 161 280 atoms) were considered to study the size effect on the mechanical behaviors of the monolayer qHPF. As for each tensile test, five independent simulations were conducted to reduce the uncertainty from the thermal perturbation. In general, we find that the elastic moduli, tensile strength, and fracture strain in the x direction of monolayer qHPF are all smaller than those in the y direction, regardless of the membrane size. This finding is consistent with the DFT results in Fig. 2.

In Fig. 7(b)–(d) we show the tensile modulus, tensile strength and fracture strain extracted from the stress–strain curves by averaging the corresponding results of five independent simulations. It can be seen that the tensile modulus of monolayer qHPF is almost independent of the membrane size. The values of tensile modulus in x and y directions are 161.9 ± 1.2 GPa and 224.6 ± 2.1 GPa, respectively. The tensile modulus of monolayer qHPF extracted from the present MD simulations is close to that obtained in the above DFT calculations. In contrast, the tensile strength and fracture strain obtained from the present MLP-based MD simulations are greatly smaller than those extracted from DFT calculations. For instance, for the monolayer qHPF membrane with a length of 33 nm, the tensile strengths in x and y directions predicted from MD simulations are 3.8 ± 0.1 GPa and 8.1 ± 0.1 GPa, respectively, which are only 42.6% and 55.1% of the corresponding results extracted from DFT calculations (see Fig. 2). The fracture strains of this membrane are predicted to be 2.46 ± 0.04% and 3.68 ± 0.07% in x and y directions, respectively, which are only 37.8% and 46.0% of the corresponding DFT values. The much smaller tensile strength and fracture strain predicted from MLP-based MD simulations can be attributed to the temperature and size effects, both of which are absent in previous DFT calculations. The thermal fluctuations at the finite temperature can accelerate the breaking of some C–C bonds and thus fracture of monolayer qHPF. Moreover, as the membrane length grows, the breaking probability of the C–C bonds due to thermal fluctuations increases, which results in the decrease of the tensile strength and fracture strain. Indeed, as shown in Fig. 7(c)–(d), both the tensile strength and fracture strain decrease when the membrane length increases from 5 nm to 33 nm. However, when the membrane length further grows from 33 nm to 44 nm, no significant changes are observed in both the tensile strength and fracture strain, irrespective of the loading direction. In other words, the size effects on the fracture properties of monolayer qHPF become insignificant when its length is larger than 33 nm.

3.3.2. Strain rate effect

We also investigate the effect of strain rate on the mechanical properties of monolayer qHPF at room temperature. The stress–strain curves of the monolayer qHPF membrane having the length of 33 nm × 33 nm obtained under the tension with the strain rate ranging from 1×10^7/s to 1×10^9/s are shown in Fig. 8(a). As shown in Fig. 8(b), the strain rate shows a small effect on the tensile modulus of monolayer qHPF. However, Fig. 8(c) and (d) indicate a significant enhancement effect of the strain rate on both the tensile strength and fracture strain of monolayer qHPF. For instance, the tensile strengths in x and y directions increase from 3.6 ± 0.1 GPa to 4.2 ± 0.0 GPa and from 7.1 ± 0.2 GPa to 9.0 ± 0.1 GPa, respectively, when the strain rate grows from 1×10^7/s to 1×10^9/s. The enhancement effect of strain rate on the fracture properties can be understood by the following reason. The atoms of monolayer qHPF at a higher strain rate have less time to respond to the loading. Thus, there is a less chance for the atoms to overcome the energy barrier and trigger the breaking of bonds, which results in a larger tensile strength and fracture strain. Theoretically, the tensile strength and strain rate can be represented by $\sigma_f = C\dot{\epsilon}^m$ [68], where σ_f, $\dot{\epsilon}$, m, and C denote the rate-independent tensile strength, strain rate, the strain-rate sensitivity, and a constant, respectively. As shown in Fig. 8(c), our MD simulation results agree well with this theoretical prediction. Specifically, we find that the tensile strength in the y direction is more sensitive to the strain rate. Moreover, the rate-independent tensile strength along x and y directions are extrapolated to be 3.58 GPa and 7.09 GPa, respectively.

3.3.3. Temperature effect

In the above discussion we find that due to the thermal fluctuation, the mechanical properties of monolayer qHPF should be dependent on the temperature. To further investigate the temperature effect, the uniaxial tensile simulations were conducted at eight different temperatures ranging from 100 K to

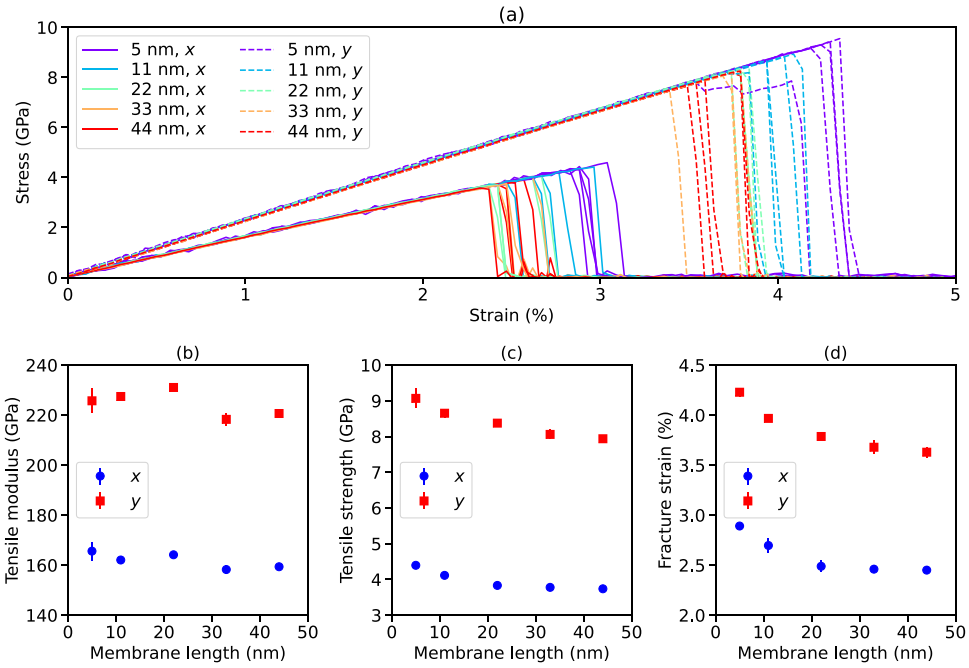

Fig. 7. (a) Stress–strain curves of monolayer qHPF membrane with different sizes under uniaxial tension in both x and y directions. Here, results of five independent simulations were presented for each membrane. (b) Tensile modulus, (c) tensile strength, and (d) fracture strain of the monolayer qHPF membrane with different sizes.

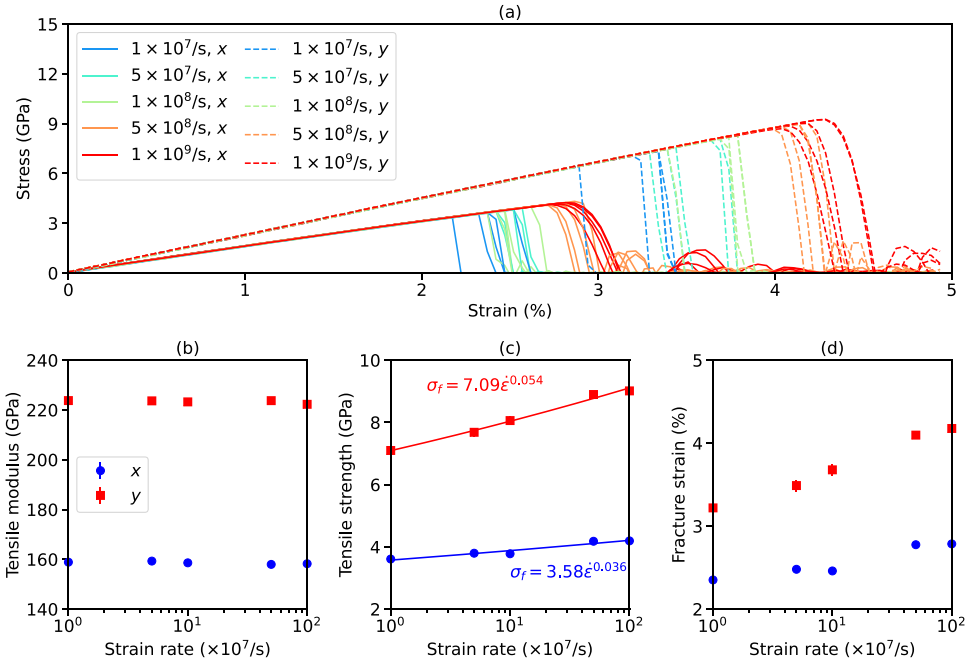

Fig. 8. Stress–strain curves of monolayer qHPF membrane uniaxially stretched along both x and y directions with different strain rates. Here, results of five independent simulations were presented for each membrane. (b) Tensile modulus, (c) tensile strength, and (d) fracture strain of monolayer qHPF stretched with different strain rates.

800 K for the monolayer qHPF membrane with the size of 33 nm × 33 nm. Similarly, five independent simulations were conducted at each temperature with the same strain rate of 1×10^8/s. The obtained strain–stress curves at different temperatures are shown in Fig. 9(a), based on which the tensile moduli, tensile strengths and fracture strains at different temperature were evaluated.

As shown in Fig. 9(b), when the temperature increases from 100 K to 800 K, the tensile modulus in x and y directions of monolayer qHPF, respectively, decrease from 163.2 ± 0.5 GPa to 146.3 ± 4.2 GPa and from 230.7 ± 0.4 GPa to 190.2 ± 5.8 GPa due to the so-called thermally induced softening effect widely observed in many other 2D materials [69–71]. The tensile strength and fracture strain are found to similarly decrease as the temperature grows. This is because covalent bonds in monolayer qHPF exhibit a more significant thermal fluctuation at a higher temperature. In other words, the high atomic kinetic energy and mobility at the high temperature can cause a more deviated distance between carbon atoms as depicted in Fig. 10. Once some inter-fullerene bonds break due the serious thermal fluctuation at the high temperature, the fracture is initiated immediately

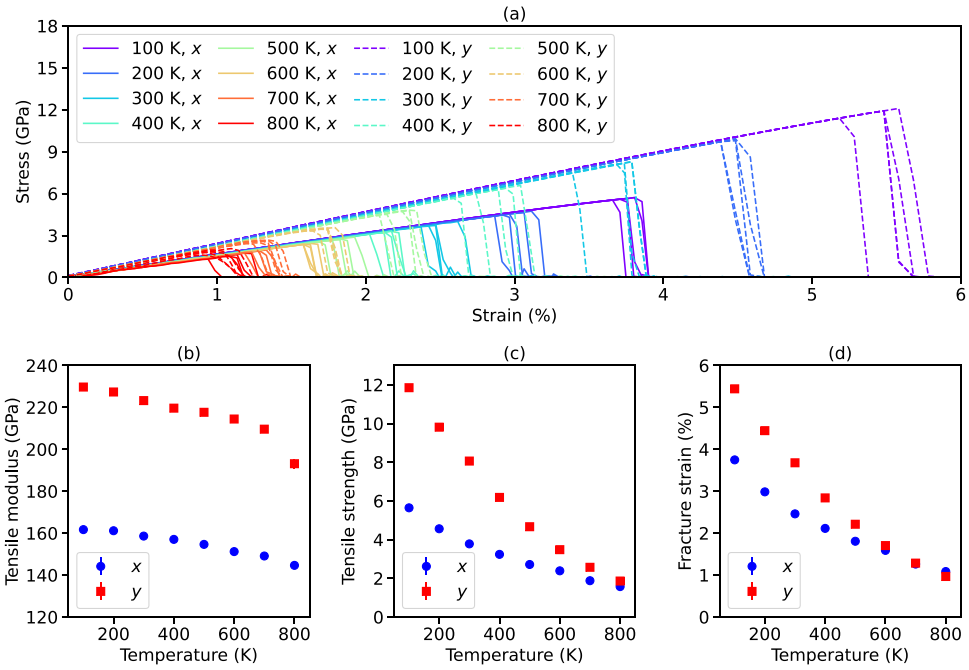

Fig. 9. (a) Stress–strain curves of monolayer qHPF membrane at different temperatures under uniaxial tension in both x and y directions. Here, results of five independent simulations were presented for each membrane. (b) Tensile modulus, (c) tensile strength, and (d) fracture strain of monolayer qHPF at different temperatures.

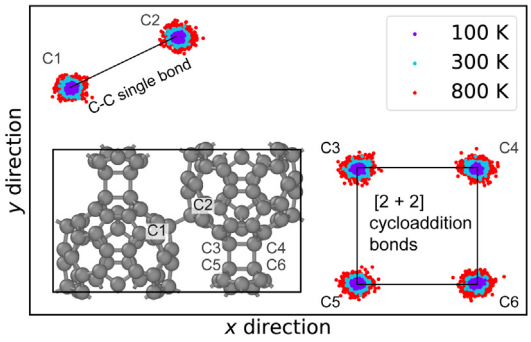

Fig. 10. A comparison among the atomic trajectories of inter-fullerene covalent bonds in qHPF at different temperatures.

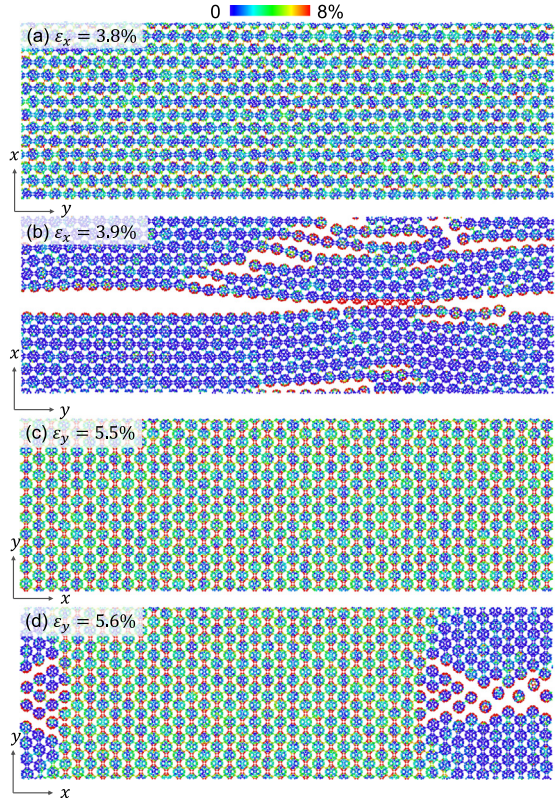

Fig. 11. The snapshots sampled at specific strains before and after fracture of qHPF with a size of 33 nm × 33 nm under tension at 100 K. The atoms in the snapshots were colored based on their atomic volumetric strains using the OVITO package [40]. The strain in (a, b) is the component in the x direction of qHPF stretched along the x direction, while the result in (c, d) is the strain component in the y direction of qHPF stretched along the y direction. (For interpretation of the references to color in this figure legend, the reader is referred to the web version of this article.)

followed by the catastrophic failure of the entire monolayer qHPF. Comparing the temperature effect on the fracture properties in x and y directions, the tensile strength and fracture strain in the y direction is more sensitive to the temperature change. For example, at a relatively low temperature of 100 K, the tensile strength in the y direction is 11.85 ± 0.11 GPa as about twice as 5.64 ± 0.03 GPa in the x direction. However, due to its more sensitivity to the temperature change, the tensile strength in the y direction decreases to 1.86 ± 0.07 GPa at 800 K that is comparable to the value (1.57 ± 0.06 GPa) in the x direction at the same temperature. Similarly, although at the temperature of 100 K the fracture strain in the y direction is about 45.1% larger than that in the x direction, the fracture strains in these two direction are found to extremely close to each other at 700 K. Furthermore, as the temperature keeps growing to 800 K, the fracture strain in the x direction eventually turns to be much larger than its counterpart in the y direction.

In Fig. 11, we show the atomic strain distributions in the monolayer qHPF stretched along x and y directions just before and after fracture. From Fig. 11(a), it can be found that the deformation of monolayer qHPF under the tension in the x direction

majorly originates from the elongation of the inter-fullerene C–C single bonds, where the largest atomic strain is often observed. Similarly, as shown in Fig. 11(c), the elongation of [2 + 2] cycloaddition bonds majorly contributes to the deformation of monolayer qHPF under the tension in the *y* direction. These findings further prove the significant inhomogeneous deformation of the stretched monolayer qHPF, irrespective of the loading direction. Moreover, as shown in Fig. 11(b) and (c), the crack of the qHPF membrane stretched along the *x* direction exhibits a straight-line pattern that is parallel to the loading direction, while edges of the crack of the membrane stretched along the *y* direction could have a more complicated zigzag pattern. The different crack patterns of monolayer qHPF stretched along different directions are consist with the results predicted in the above DFT calculations. Finally, it is worth mentioning that due to the thermal fluctuation, the monolayer qHPF utilized at a finite temperature possesses a fracture strain much smaller than that predicted from above DFT calculations as shown in Fig. 2 at the absolute zero temperature. Actually, as shown in Fig. 3, due to the effect of some factors in reality such as the size and temperature effects, the tensile strength and fracture strain of 2D materials measured in experiments are generally smaller than those predicted from DFT calculations. These practical factors actually can be taken into account in MLP-based MD simulations, which also hold the accuracy comparable to DFT calculations. Indeed, the tensile strength and fracture strain of monolayer qHPF predicted from MLP-based MD are generally smaller than their DFT calculation results (see Fig. 3). Thus, as shown in Fig. S2 (see supplemental material), when the strain engineering is used to modify the electronic properties of monolayer qHPF in practice, it is necessary to strictly keep the applied strain smaller than the fracture strain.

4. Summary and conclusions

In summary, we have constructed an accurate MLP based on the efficient NEP approach for the monolayer qHPF. Compared with both the DFT and empirical potentials approaches, the NEP model is superior in determining mechanical behaviors of the monolayer qHPF under uniaxial tension, because it can consider the effects of membrane size and finite temperature in the real environment. The mechanical properties including tensile modulus, tensile strength and fracture strain of monolayer qHPF are found to be strongly anisotropic, which is due to the distinct properties of different inter-fullerene bonds. Most notably, it is found that the tensile strength and fracture strain of monolayer qHPF are much smaller than any other existing 2D carbon crystals. This mechanical fragility originates from the inhomogeneous deformation of the stretched monolayer qHPF, since the soft inter-fullerene bonds and the rigid fullerenes have different siffnesses. Overall, this work not only provides an atomistic insight into the mechanical anisotropy and fracture behaviors of monolayer qHPF, but also demonstrates the effectiveness and accuracy of machine-learned NEP-based MD simulations in simulating the mechanical behaviors of 2D materials with considering more realistic factors such as size and thermal effects.

CRediT authorship contribution statement

Penghua Ying: Conceptualization, Methodology, Software, Formal analysis, Writing – original draft, Writing – review & editing. **Haikuan Dong:** Methodology, Software, Formal analysis. **Ting Liang:** Software, Formal analysis. **Zheyong Fan:** Methodology, Formal analysis, Writing – review & editing. **Zheng Zhong:** Supervision, Resources, Funding acquisition, Writing – review & editing. **Jin Zhang:** Conceptualization, Investigation, Software, Formal analysis, Writing – original draft, Writing – review & editing.

Declaration of competing interest

The authors declare that they have no known competing financial interests or personal relationships that could have appeared to influence the work reported in this paper.

Data availability

Complete input and output files for the NEP training and testing are freely available at a Zenodo repository (http://dx.doi.org/10.5281/zenodo.7018573).

Acknowledgments

P.Y. thanks Xiaowen Li and Xiaobin Qiang for discussions. Z.F. acknowledges support from the National Natural Science Foundation of China (No. 11974059). Z.Z. acknowledges the National Natural Science Foundation of China (Grant No. 11932005) and the program of Innovation Team in Universities and Colleges in Guangdong (2021KCXTD006). J.Z. acknowledges the support from the Guangdong Basic and Applied Basic Research Foundation (No. 2022A1515010631).

Appendix A. Supplementary data

Supplementary material related to this article can be found online at https://doi.org/10.1016/j.eml.2022.101929.

References

[1] H.W. Kroto, J.R. Heath, S.C. O'Brien, R.F. Curl, R.E. Smalley, C60: Buckminsterfullerene, Nature 318 (6042) (1985) 162–163, http://dx.doi.org/10.1038/318162a0.
[2] L. Shi, P. Rohringer, K. Suenaga, Y. Niimi, J. Kotakoski, J.C. Meyer, H. Peterlik, M. Wanko, S. Cahangirov, A. Rubio, et al., Confined linear carbon chains as a route to bulk carbyne, Nature Mater. 15 (6) (2016) 634–639, http://dx.doi.org/10.1038/nmat4617.
[3] S. Iijima, Helical microtubules of graphitic carbon, Nature 354 (6348) (1991) 56–58, http://dx.doi.org/10.1038/354056a0.
[4] K.S. Novoselov, A.K. Geim, S.V. Morozov, D.-e. Jiang, Y. Zhang, S.V. Dubonos, I.V. Grigorieva, A.A. Firsov, Electric field effect in atomically thin carbon films, Science 306 (5696) (2004) 666–669, http://dx.doi.org/10.1126/science.1102896.
[5] S. Margadonna, K. Prassides, Recent advances in fullerene superconductivity, J. Solid State Chem. 168 (2) (2002) 639–652, http://dx.doi.org/10.1006/jssc.2002.9762.
[6] C. Liu, H.-M. Cheng, Controlled growth of semiconducting and metallic single-wall carbon nanotubes, J. Am. Chem. Soc. 138 (21) (2016) 6690–6698, http://dx.doi.org/10.1021/jacs.6b00838.
[7] C. Lee, X. Wei, J.W. Kysar, J. Hone, Measurement of the elastic properties and intrinsic strength of monolayer graphene, Science 321 (5887) (2008) 385–388, http://dx.doi.org/10.1126/science.1157996.
[8] E. Gao, Y. Guo, Z. Wang, S.O. Nielsen, R.H. Baughman, The strongest and toughest predicted materials: Linear atomic chains without a peierls instability, Matter 5 (4) (2022) 1192–1203, http://dx.doi.org/10.1016/j.matt.2022.01.021.
[9] E. Gao, R. Li, R.H. Baughman, Predicted confinement-enhanced stability and extraordinary mechanical properties for carbon nanotube wrapped chains of linear carbon, ACS Nano 14 (12) (2020) 17071–17079, http://dx.doi.org/10.1021/acsnano.0c06602.
[10] A.A. Balandin, D.L. Nika, Phononics in low-dimensional materials, Mater. Today 15 (6) (2012) 266–275, http://dx.doi.org/10.1016/S1369-7021(12)70117-7.
[11] Q.H. Wang, D.O. Bellisario, L.W. Drahushuk, R.M. Jain, S. Kruss, M.P. Landry, S.G. Mahajan, S.F. Shimizu, Z.W. Ulissi, M.S. Strano, Low dimensional carbon materials for applications in mass and energy transport, Chem. Mater. 26 (1) (2014) 172–183, http://dx.doi.org/10.1021/cm402895e.
[12] J. Romo-Herrera, M. Terrones, H. Terrones, S. Dag, V. Meunier, Covalent 2D and 3D networks from 1D nanostructures: designing new materials, Nano Lett. 7 (3) (2007) 570–576, http://dx.doi.org/10.1021/nl0622202.
[13] X. Gao, X. Shen, Face-to-face crosslinking of graphdiyne and related carbon sheets toward integrated graphene nanoribbon arrays, Carbon 125 (2017) 536–543, http://dx.doi.org/10.1016/j.carbon.2017.09.097.

[14] G. Yu, L. Jiang, Y. Zheng, Surface magnetism of the carbon foam: An ab-initio theoretical study, Appl. Phys. Lett. 105 (6) (2014) 061601, http://dx.doi.org/10.1063/1.4892916.

[15] A.N. Andriotis, M. Menon, R.M. Sheetz, L. Chernozatonskii, Magnetic properties of C60 polymers, Phys. Rev. Lett. 90 (2) (2003) 026801, http://dx.doi.org/10.1103/PhysRevLett.90.026801.

[16] E. Tylianakis, G.K. Dimitrakakis, F.J. Martin-Martinez, S. Melchor, J.A. Dobado, E. Klontzas, G.E. Froudakis, Designing novel nanoporous architectures of carbon nanotubes for hydrogen storage, Int. J. Hydrogen Energy 39 (18) (2014) 9825–9829, http://dx.doi.org/10.1016/j.ijhydene.2014.03.011.

[17] C. Zhang, A. Akbarzadeh, W. Kang, J. Wang, A. Mirabolghasemi, Nano-architected metamaterials: carbon nanotube-based nanotrusses, Carbon 131 (2018) 38–46, http://dx.doi.org/10.1016/j.carbon.2018.01.082.

[18] N.V. Krainyukova, E.N. Zubarev, Carbon honeycomb high capacity storage for gaseous and liquid species, Phys. Rev. Lett. 116 (5) (2016) 055501, http://dx.doi.org/10.1103/PhysRevLett.116.055501.

[19] J. Zhang, C. Wang, Buckling of carbon honeycombs: a new mechanism for molecular mass transportation, J. Phys. Chem. C 121 (14) (2017) 8196–8203, http://dx.doi.org/10.1021/acs.jpcc.7b00716.

[20] L. Hou, X. Cui, B. Guan, S. Wang, R. Li, Y. Liu, D. Zhu, J. Zheng, Synthesis of a monolayer fullerene network, Nature 606 (7914) (2022) 507–510, http://dx.doi.org/10.1038/s41586-022-04771-5.

[21] Y. Iwasa, T. Arima, R. Fleming, T. Siegrist, O. Zhou, R. Haddon, L. Rothberg, K. Lyons, H. Carter Jr., A. Hebard, et al., New phases of C60 synthesized at high pressure, Science 264 (5165) (1994) 1570–1572, http://dx.doi.org/10.1126/science.264.5165.1570.

[22] V. Belavin, L. Bulusheva, A. Okotrub, D. Tomanek, Stability, electronic structure and reactivity of the polymerized fullerite forms, J. Phys. Chem. Solids 61 (12) (2000) 1901–1911, http://dx.doi.org/10.1016/S0022-3697(00)00079-2.

[23] A. Okotrub, V. Belavin, L. Bulusheva, V. Davydov, T. Makarova, D. Tománek, Electronic structure and properties of rhombohedrally polymerized C60, J. Chem. Phys. 115 (12) (2001) 5637–5641, http://dx.doi.org/10.1063/1.1398079.

[24] V. Belavin, L. Bulusheva, A. Okotrub, T. Makarova, Magnetic ordering in C60 polymers with partially broken intermolecular bonds, Phys. Rev. B 70 (15) (2004) 155402, http://dx.doi.org/10.1103/PhysRevB.70.155402.

[25] B. Mortazavi, X. Zhuang, Low and anisotropic tensile strength and thermal conductivity in the single-layer fullerene network predicted by machine-learning interatomic potentials, Coatings 12 (8) (2022) 1171, http://dx.doi.org/10.3390/coatings12081171.

[26] R.M. Tromer, L.A.R. Junior, D.S. Galvão, A DFT study of the electronic, optical, and mechanical properties of a recently synthesized monolayer fullerene network, Chem. Phys. Lett. (2022) 139925, http://dx.doi.org/10.1016/j.cplett.2022.139925.

[27] E. Scalise, M. Houssa, G. Pourtois, V. Afanas'ev, A. Stesmans, Strain-induced semiconductor to metal transition in the two-dimensional honeycomb structure of MoS2, Nano Res. 5 (1) (2012) 43–48, http://dx.doi.org/10.1007/s12274-011-0183-0.

[28] P. Ying, X. Li, X. Qiang, Y. Du, J. Zhang, L. Chen, Z. Zhong, Tension-induced phase transformation and anomalous Poisson effect in violet phosphorene, Mater. Today Phys. 27 (2022) 100755, http://dx.doi.org/10.1016/j.mtphys.2022.100755.

[29] S. Yang, Y. Chen, C. Jiang, Strain engineering of two-dimensional materials: methods, properties, and applications, InfoMat 3 (4) (2021) 397–420, http://dx.doi.org/10.1002/inf2.12177.

[30] Z. Dai, L. Liu, Z. Zhang, Strain engineering of 2D materials: issues and opportunities at the interface, Adv. Mater. 31 (45) (2019) 1805417, http://dx.doi.org/10.1002/adma.201805417.

[31] D. Akinwande, C.J. Brennan, J.S. Bunch, P. Egberts, J.R. Felts, H. Gao, R. Huang, J.-S. Kim, T. Li, Y. Li, et al., A review on mechanics and mechanical properties of 2d materials—Graphene and beyond, Extreme Mech. Lett. 13 (2017) 42–77, http://dx.doi.org/10.1016/j.eml.2017.01.008.

[32] J. Wu, E. Zhou, Z. Qin, X. Zhang, G. Qin, Accessing negative Poisson's ratio of graphene by machine learning interatomic potentials, Nanotechnology 33 (27) (2022) 275710, http://dx.doi.org/10.1088/1361-6528/ac5cfd.

[33] M. Wen, E.B. Tadmor, Hybrid neural network potential for multilayer graphene, Phys. Rev. B 100 (19) (2019) 195419, http://dx.doi.org/10.1103/PhysRevB.100.195419.

[34] B. Mortazavi, I.S. Novikov, A.V. Shapeev, A machine-learning-based investigation on the mechanical/failure response and thermal conductivity of semiconducting BC2N monolayers, Carbon 188 (2022) 431–441, http://dx.doi.org/10.1016/j.carbon.2021.12.039.

[35] B. Mortazavi, M. Silani, E.V. Podryabinkin, T. Rabczuk, X. Zhuang, A.V. Shapeev, First-principles multiscale modeling of mechanical properties in graphene/borophene heterostructures empowered by machine-learning interatomic potentials, Adv. Mater. 33 (35) (2021) 2102807, http://dx.doi.org/10.1002/adma.202102807.

[36] Z. Fan, Z. Zeng, C. Zhang, Y. Wang, K. Song, H. Dong, Y. Chen, T. Ala-Nissila, Neuroevolution machine learning potentials: Combining high accuracy and low cost in atomistic simulations and application to heat transport, Phys. Rev. B 104 (10) (2021) 104309, http://dx.doi.org/10.1103/PhysRevB.104.104309.

[37] Z. Fan, Improving the accuracy of the neuroevolution machine learning potential for multi-component systems, J. Phys.: Condens. Matter 34 (12) (2022) 125902, http://dx.doi.org/10.1088/1361-648X/ac462b.

[38] Z. Fan, Y. Wang, P. Ying, K. Song, J. Wang, Y. Wang, Z. Zeng, K. Xu, E. Lindgren, J.M. Rahm, A.J. Gabourie, J. Liu, H. Dong, J. Wu, Y. Chen, Z. Zhong, J. Sun, P. Erhart, Y. Su, T. Ala-Nissila, GPUMD: A package for constructing accurate machine-learned potentials and performing highly efficient atomistic simulations, J. Chem. Phys. 157 (11) (2022) 114801, http://dx.doi.org/10.1063/5.0106617.

[39] K. Momma, F. Izumi, VESTA 3 for three-dimensional visualization of crystal, volumetric and morphology data, J. Appl. Crystallogr. 44 (6) (2011) 1272–1276, http://dx.doi.org/10.1107/S0021889811038970.

[40] A. Stukowski, Visualization and analysis of atomistic simulation data with OVITO–the open visualization tool, Modelling Simulation Mater. Sci. Eng. 18 (1) (2009) 015012, http://dx.doi.org/10.1088/0965-0393/18/1/015012.

[41] G. Kresse, J. Furthmüller, Efficient iterative schemes for ab initio total-energy calculations using a plane-wave basis set, Phys. Rev. B 54 (16) (1996) 11169, http://dx.doi.org/10.1103/PhysRevB.54.11169.

[42] J.P. Perdew, K. Burke, M. Ernzerhof, Generalized gradient approximation made simple, Phys. Rev. Lett. 77 (18) (1996) 3865, http://dx.doi.org/10.1103/PhysRevLett.77.3865.

[43] P.E. Blöchl, Projector augmented-wave method, Phys. Rev. B 50 (24) (1994) 17953, http://dx.doi.org/10.1103/PhysRevB.50.17953.

[44] T. Schaul, T. Glasmachers, J. Schmidhuber, High dimensions and heavy tails for natural evolution strategies, in: Proceedings of the 13th Annual Conference on Genetic and Evolutionary Computation, GECCO '11, Association for Computing Machinery, New York, NY, USA, 2011, pp. 845–852, http://dx.doi.org/10.1145/2001576.2001692.

[45] J. Behler, M. Parrinello, Generalized neural-network representation of high-dimensional potential-energy surfaces, Phys. Rev. Lett. 98 (2007) 146401, http://dx.doi.org/10.1103/PhysRevLett.98.146401.

[46] Z. Fan, W. Chen, V. Vierimaa, A. Harju, Efficient molecular dynamics simulations with many-body potentials on graphics processing units, Comput. Phys. Comm. 218 (2017) 10–16, http://dx.doi.org/10.1016/j.cpc.2017.05.003.

[47] H.J. Berendsen, J.v. Postma, W.F. Van Gunsteren, A. DiNola, J.R. Haak, Molecular dynamics with coupling to an external bath, J. Chem. Phys. 81 (8) (1984) 3684–3690, http://dx.doi.org/10.1063/1.448118.

[48] G. Bussi, D. Donadio, M. Parrinello, Canonical sampling through velocity rescaling, J. Chem. Phys. 126 (1) (2007) 014101, http://dx.doi.org/10.1063/1.2408420.

[49] M. Bernetti, G. Bussi, Pressure control using stochastic cell rescaling, J. Chem. Phys. 153 (11) (2020) 114107, http://dx.doi.org/10.1063/5.0020514.

[50] B. Silvi, A. Savin, Classification of chemical bonds based on topological analysis of electron localization functions, Nature 371 (6499) (1994) 683–686, http://dx.doi.org/10.1038/371683a0.

[51] F. Liu, P. Ming, J. Li, Ab initio calculation of ideal strength and phonon instability of graphene under tension, Phys. Rev. B 76 (6) (2007) 064120, http://dx.doi.org/10.1103/PhysRevB.76.064120.

[52] K. Cao, S. Feng, Y. Han, L. Gao, T. Hue Ly, Z. Xu, Y. Lu, Elastic straining of free-standing monolayer graphene, Nature Commun. 11 (1) (2020) 1–7, http://dx.doi.org/10.1038/s41467-019-14130-0.

[53] J. Wu, B. Wang, Y. Wei, R. Yang, M. Dresselhaus, Mechanics and mechanically tunable band gap in single-layer hexagonal boron-nitride, Mater. Res. Lett. 1 (4) (2013) 200–206, http://dx.doi.org/10.1080/21663831.2013.824516.

[54] A. Falin, Q. Cai, E.J. Santos, D. Scullion, D. Qian, R. Zhang, Z. Yang, S. Huang, K. Watanabe, T. Taniguchi, et al., Mechanical properties of atomically thin boron nitride and the role of interlayer interactions, Nature Commun. 8 (1) (2017) 1–9, http://dx.doi.org/10.1038/ncomms15815.

[55] Q. Peng, W. Ji, S. De, Mechanical properties of graphyne monolayers: a first-principles study, Phys. Chem. Chem. Phys. 14 (38) (2012) 13385–13391, http://dx.doi.org/10.1039/C2CP42387A.

[56] B. Mortazavi, A.V. Shapeev, Anisotropic mechanical response, high negative thermal expansion, and outstanding dynamical stability of biphenylene monolayer revealed by machine-learning interatomic potentials, FlatChem 32 (2022) 100347, http://dx.doi.org/10.1016/j.flatc.2022.100347.

[57] H. Wang, Q. Li, Y. Gao, F. Miao, X.-F. Zhou, X. Wan, Strain effects on borophene: ideal strength, negative possion's ratio and phonon instability, New J. Phys. 18 (7) (2016) 073016, http://dx.doi.org/10.1088/1367-2630/18/7/073016.

[58] Q. Peng, X. Wen, S. De, Mechanical stabilities of silicene, Rsc Adv. 3 (33) (2013) 13772–13781, http://dx.doi.org/10.1039/C3RA41347K.

[59] Q. Wei, X. Peng, Superior mechanical flexibility of phosphorene and few-layer black phosphorus, Appl. Phys. Lett. 104 (25) (2014) 251915, http://dx.doi.org/10.1063/1.4885215.

[60] T. Li, Ideal strength and phonon instability in single-layer MoS2, Phys. Rev. B 85 (23) (2012) 235407, http://dx.doi.org/10.1103/PhysRevB.85.235407.
[61] V.L. Deringer, G. Csányi, Machine learning based interatomic potential for amorphous carbon, Phys. Rev. B 95 (9) (2017) 094203, http://dx.doi.org/10.1103/PhysRevB.95.094203.
[62] H. Dong, C. Cao, P. Ying, Z. Fan, P. Qian, Y. Su, Anisotropic and high thermal conductivity in monolayer quasi-hexagonal fullerene: A comparative study against bulk phase fullerene, 2022, http://dx.doi.org/10.48550/arXiv.2208.03982.
[63] J. Tersoff, Modeling solid-state chemistry: Interatomic potentials for multicomponent systems, Phys. Rev. B 39 (1989) 5566–5568, http://dx.doi.org/10.1103/PhysRevB.39.5566.
[64] L. Lindsay, D.A. Broido, Optimized tersoff and brenner empirical potential parameters for lattice dynamics and phonon thermal transport in carbon nanotubes and graphene, Phys. Rev. B 81 (2010) 205441, http://dx.doi.org/10.1103/PhysRevB.81.205441.
[65] D.W. Brenner, Empirical potential for hydrocarbons for use in simulating the chemical vapor deposition of diamond films, Phys. Rev. B 42 (15) (1990) 9458, http://dx.doi.org/10.1103/PhysRevB.42.9458.
[66] J. Los, A. Fasolino, Intrinsic long-range bond-order potential for carbon: Performance in Monte Carlo simulations of graphitization, Phys. Rev. B 68 (2) (2003) 024107, http://dx.doi.org/10.1103/PhysRevB.68.024107.
[67] J.P. Janet, C. Duan, T. Yang, A. Nandy, H.J. Kulik, A quantitative uncertainty metric controls error in neural network-driven chemical discovery, Chem. Sci. 10 (34) (2019) 7913–7922, http://dx.doi.org/10.1039/c9sc02298h.
[68] G.E. Dieter, D. Bacon, Mechanical Metallurgy, Vol. 3, McGraw-hill New York, 1976.
[69] M. Chen, S. Quek, Z. Sha, C. Chiu, Q. Pei, Y. Zhang, Effects of grain size, temperature and strain rate on the mechanical properties of polycrystalline graphene–A molecular dynamics study, Carbon 85 (2015) 135–146, http://dx.doi.org/10.1016/j.carbon.2014.12.092.
[70] Z.-D. Sha, Q.-X. Pei, Z. Ding, J.-W. Jiang, Y.-W. Zhang, Mechanical properties and fracture behavior of single-layer phosphorene at finite temperatures, J. Phys. D: Appl. Phys. 48 (39) (2015) 395303, http://dx.doi.org/10.1088/0022-3727/48/39/395303.
[71] A.S.M.J. Islam, M.S. Akbar, M.S. Islam, J. Park, Temperature- and defect-induced uniaxial tensile mechanical behaviors and the fracture mechanism of two-dimensional silicon germanide, ACS Omega 6 (34) (2021) 21861–21871, http://dx.doi.org/10.1021/acsomega.1c01691.